JVST B
Journal of Vacuum Science & Technology B

Neural optoelectrodes merging semiconductor scalability with polymeric-like bendability for low damage acute *in vivo* neuron readout and stimulation

Cite as: J. Vac. Sci. Technol. B **39**, 063001 (2021); https://doi.org/10.1116/6.0001269
Submitted: 08 July 2021 • Accepted: 24 September 2021 • Published Online: 23 November 2021

Vittorino Lanzio, Vanessa Gutierrez, John Hermiz, et al.

COLLECTIONS

Paper published as part of the special topic on 64th International Conference on Electron, Ion, And Photon Beam Technology and Nanofabrication, EIPBN 2021

This paper was selected as Featured

ARTICLES YOU MAY BE INTERESTED IN

Long-term brain-on-chip: Multielectrode array recordings in 3D neural cell cultures
Journal of Vacuum Science & Technology B **39**, 064004 (2021); https://doi.org/10.1116/6.0001297

100 keV vacuum sealed field emission gun for high resolution electron microscopy
Journal of Vacuum Science & Technology B **39**, 062804 (2021); https://doi.org/10.1116/6.0001275

Diffraction-grating beam splitter, interferometric-lithography nanopatterning with a multilongitudinal-mode diode laser
Journal of Vacuum Science & Technology B **39**, 062603 (2021); https://doi.org/10.1116/6.0001377

© 2021 Author(s).

ARTICLE

avs.scitation.org/journal/jvb

Neural optoelectrodes merging semiconductor scalability with polymeric-like bendability for low damage acute *in vivo* neuron readout and stimulation

Cite as: J. Vac. Sci. Technol. B **39**, 063001 (2021); doi: 10.1116/6.0001269
Submitted: 8 July 2021 · Accepted: 24 September 2021 ·
Published Online: 23 November 2021

View Online Export Citation CrossMark

Vittorino Lanzio,[1,2,a)] Vanessa Gutierrez,[3] John Hermiz,[3,4] Kristofer Bouchard,[3,4,5,6] and Stefano Cabrini[1,a)]

AFFILIATIONS

[1]The Molecular Foundry, Lawrence Berkeley National Laboratory, Berkeley, California 94720
[2]Department of Applied Science and Technology, Politecnico di Torino, Torino 10129, Italy
[3]Biological Systems and Engineering Division, Lawrence Berkeley National Laboratory, Berkeley, California 94720
[4]Redwood Center for Theoretical Neuroscience, University of California, Berkeley, California 94720
[5]Computational Research Divisions, Lawrence Berkeley National Laboratory, Berkeley, California 94720
[6]Helen Wills Neuroscience Institute, University of California, Berkeley, California 94720

Note: This paper is part of the Special Collection: 64th International Conference on Electron, Ion, And Photon Beam Technology and Nanofabrication, EIPBN 2021.

[a)]**Authors to whom correspondence should be addressed:** vittorinolanzio@lbl.gov; vitto.lanzio@gmail.com; and scabrini@lbl.gov

ABSTRACT

Neural optoelectrodes can read and manipulate large numbers of neurons *in vivo*. However, state-of-the-art devices rely on either standard microfabrication materials (i.e., silicon and silicon nitride), which result in high scalability and throughput but cause severe brain damage due to implant stiffness, or polymeric devices, which are more compliant but whose scalability and implantation in the brain are challenging. Here, we merge the gap between silicon-based fabrication scalability and low (polymeric-like) stiffness by fabricating a nitride and oxide-based optoelectrode with a high density of sensing microelectrodes, passive photonic circuits, and a very small tip thickness (5 μm). We achieve this by removing all the silicon supporting material underneath the probe's tip—while leaving only the nitride and glass optical ultrathin layers—through a single isotropic etch step. Our optoelectrode integrates 64 electrodes and multiple passive optical outputs, resulting in a cross-sectional area coefficient (the cross section divided by the number of sensors and light emitters) of 3.1—smaller than other optoelectrodes. It also combines a low bending stiffness ($\sim 4.4 \times 10^{-11}$ N m^2), comparable or approaching several state-of-the-art polymeric optoelectrodes. We tested several mechanical insertions of our devices *in vivo* in rats and demonstrated that we can pierce the pia without using additional temporary supports.

Published under an exclusive license by the AVS. https://doi.org/10.1116/6.0001269

I. INTRODUCTION

Studying neural activity in living animals at the single neuron and network-level holds many critical industrial,[1] medical,[2,3] and neuroscientific[4–6] applications. Neural probes are invasive *in vivo* devices that consist of microcantilever tips integrating sensors and stimulation sites to read and stimulate neural activity once inserted inside the brain tissue.[7] Sensors typically consist of microelectrodes for electrophysiology measurements, while light emitters such as μLEDs or waveguides act as optogenetic stimulators. Probes integrating large numbers of electrodes can detect multiple neurons (from tens to hundreds) with single neuron and single neural event resolutions ($\sim$10 μm and sub-ms, respectively). Combining light emitters with electrodes in a single device (optoelectrode) allows for implementing recording and stimulation feedback loops in the brain.[8,9] Like electrodes, the integration of increased numbers of light emitters and the ability to address them individually allow to

Published under an exclusive license by the AVS

excite or inhibit portions of the neural network and detect the corresponding signal propagation change through the electrodes. Specifically, micro-light-emitting diodes (μLEDs) can be turned on/off by applying an electrical current but result in significant heat generation in brain tissue.[10–13] On the other hand, photonic waveguide approaches[14] allow for passive (meaning without significant heat generation) light delivery in different brain areas.

While silicon nitride-based optoelectrodes allow for integrating a high number of sensors (dozens[15–20] to hundreds[21–23]) and passive addressable light emitters (i.e., rings,[15,16] arrayed waveguide gratings,[24] or Mach–Zehnder interference switches[19]), their high Young modulus (~130–170 GPa[25]) results in a material mismatch with the surrounding brain tissue and laceration during micromotions.[26]

On the other hand, polymeric probes have low Young modulus (~1–20 GPa[26]) and thus are more flexible and reduce tissue damage,[27–29] but do not allow for integrating large numbers of polymeric waveguides, especially considering their bulky cross-sectional dimensions of hundreds of μm^2 [while silicon nitride waveguides around 0.06 μm^2 (Refs. 15, 16, and 20)]. Besides, polymeric probes are attached to temporary rigid supports for insertion in the brain, resulting in a large insertion device cross section and acute tissue damage. Other types of device architectures and materials, such as tapered optical fibers[30–32] or silicon carbide microprobes,[33,34] allow for exploring neural networks, but they, respectively, are challenging to scale or do not integrate light emitters.

In this work, we merge the gap between silicon nitride scalability and polymeric compliance by fabricating a probe with a high density of sensors, passive light emitters, and low bending stiffness, comparable (or approaching) state-of-the-art polymeric probes (Appendix A). Starting from silicon wafers—which allow for high scalability and throughput—we obtain an ultrathin (5 μm) device made of nitride and oxide optical materials by removing all supporting silicon with a single isotropic etch step. This microfabrication step removes only the silicon underneath the device's insertion area while leaving the rest of the device unaffected, allowing for its ease of handling and assembling. The resulting device integrates passive photonic circuits made of silicon nitride and oxide and embedding small footprint waveguides and optical filters[15,16]; electrode arrays are integrated above the photonics to obtain a high electrode count. In addition, the ultrasmall device cross section and the low bending stiffness allow for a reduction of brain damage during device insertion and after in the presence of brain micromotions.

We describe the parameters chosen for the probe design, the processes to nanofabricate them at the wafer-level, some *in vitro* mechanical and optical testing in saline solution and in air, and preliminary *in vivo* insertions, where we show that we can insert the device without coupling it to rigid supports, thus resulting in low device insertion damage.

Therefore, these devices and fabrication techniques provide a mix of silicon (nitride) scalability and polymericlike flexibility with a single isotropic etch step. As a result, these devices can be used for high spatiotemporal resolution acute interrogation of *in vivo* neural networks with minimal acute damage to brain tissue.

II. EXPERIMENT

A. Probe architecture

Our probe integrates both electrodes for neural readout and silicon nitride photonics for light delivery for optogenetic stimulation as shown in previous works.[15,16] However, here we significantly reduce our device's cross section to make it more flexible while keeping the same functionalities. The device is schematically illustrated in Fig. 1(a) and consists of three main areas: the tip, which is a 1 mm long, 45 μm wide, and 5 μm thick cantilever integrating the electrodes and light emitters to be inserted inside the brain of the animal to perform the experiments. This area, whose cross section is shown in Fig. 1(b), integrates the photonic elements to deliver the light in specific locations in the brain and electrodes to sense neural electrical activity. The second area is the probe's interface, which is 2 mm long, 1.5 mm wide, and 525 μm thick and where the printed circuit board (PCB) electrical and optical connections occur. Finally, the connecting area is 3–5 mm long and connects the tip to the interface area with a gradual taper in the width direction and a constant thickness of 25 μm.

Our strategy aims to remove all the silicon from the tip to reduce its cross-sectional dimensions and increase its flexibility while keeping the silicon underneath the probe's interface and connecting areas to handle and package the probe effectively. As a result, we can leverage the silicon nitride processing capabilities to integrate both high-density photonics—for example, Fig. 1(c) shows the integration of ring resonators for passive light location selection—and a high density of electrodes (64) [Fig. 1(d)].[15,16] Besides, the probe's tip is transparent [Fig. 1(e)], which opens the possibility to illuminate on both sides of the tip (Appendix B).

B. probe nanofabrication

We fabricate the probes on 4-in. wafers using micro- and nanofabrication techniques resembling the previously described ones.[15–17] Figures 2(a)–2(e) shows a schematic of the main microfabrication steps, here briefly described.

Starting from a silicon wafer with optical quality silicon oxide and nitride[35] (from Lionix) [Fig. 2(a)], we patterned the photonics with electron beam lithography and reactive ion etching (RIE), and we cladded them with 2.5 μm of silicon oxide (deposited with plasma-enhanced chemical vapor deposition) and planarized them with a flowable oxide layer (FOx) [Fig. 2(b)]. We then integrated the arrays of electrodes and interconnections for neural readout by electron beam lithography, 10 nm titanium and 100 nm gold evaporation, and liftoff; we passivated only the interconnections by depositing a 60 nm thick layer of oxide on the entire wafer and removed the passivation from the electrodes with electron beam lithography and RIE etch steps [Fig. 2(b)]. The deposition processes for the bottom and top cladding, planarization, and passivation layer will determine the final probe's tip thickness and are controlled precisely by deposition time. Next, we removed 500 μm of silicon by back etching the tip and interconnecting areas to make them 25 μm thin, leaving the interface area unaffected [Fig. 2(c)]. To do so, we performed a wet etch in potassium hydroxide using the backside nitride as a mask while protecting the wafer's front—where electrodes and wires are—with a 20 μm thick Protek B3

Published under an exclusive license by the AVS

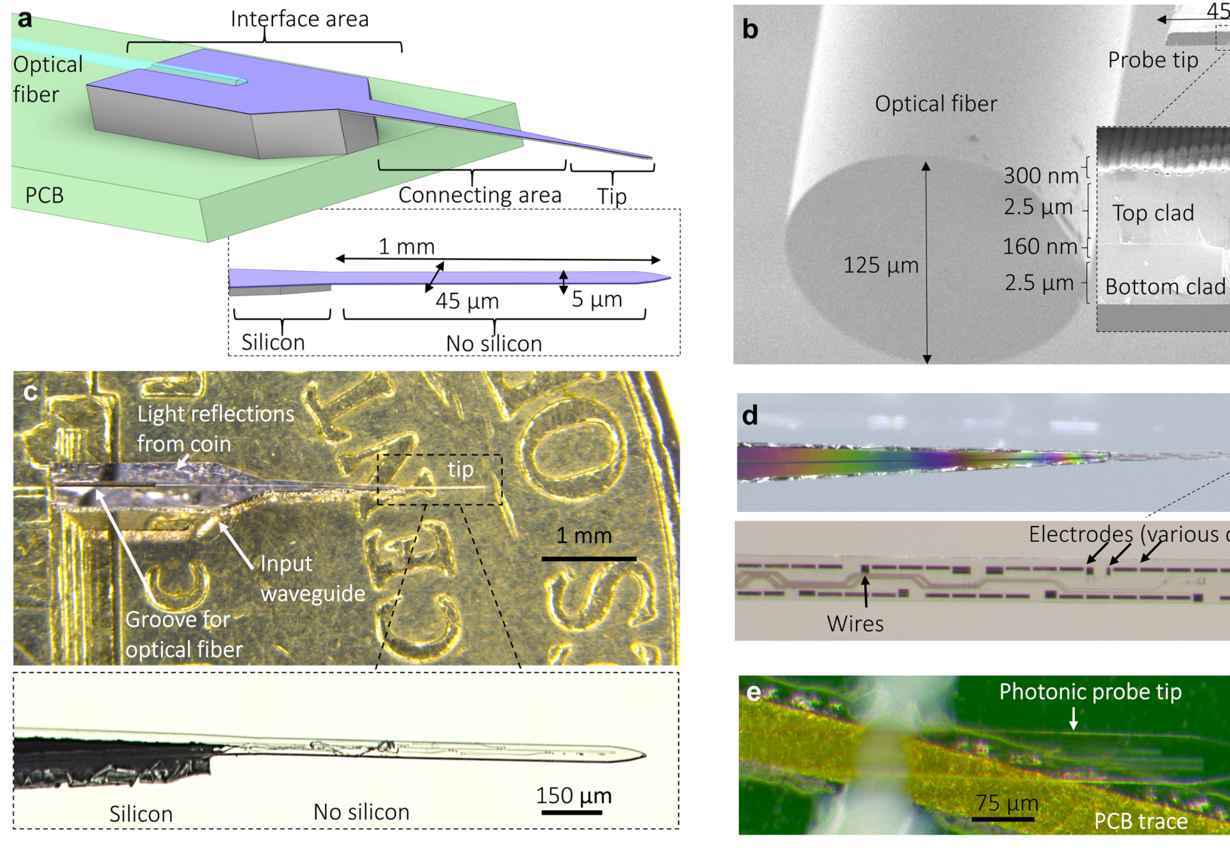

FIG. 1. Ultrathin and high-density optoelectronic neural probe. (a) Three-dimensional rendering of an optical probe, showing the interface, connecting and tip areas, and a magnification on the latter, from which we entirely remove the silicon. (b) Scanning electron microscope (SEM) cross section of a single-mode optical fiber (SM400, Thorlabs) and our probe's tip and inset showing a magnification and highlighting the nitride photonic layer and the electrodes. (c) Tilted top view optical microscope image of a photonic probe on a 5-cent U.S. coin and magnification on the tip area, which is 1 mm long, 45 μm wide, and 5 μm thick and integrating ring resonators for light delivery in brain tissue. (d) Optical microscope image of a probe's tip integrating both photonics and example of 64 electrodes with various designs. (e) Image of a photonic probe's tip on a printed circuit board, highlighting the tip's transparency inherent in its materials (silicon oxide and silicon nitride).

layer.[36] Once we obtained the photonic and electrical circuits on 25 μm thick membranes, we evaporated 30 nm of Chrome on the wafer's back. Finally, we released the devices by dry etching their shape from the wafer's front side and using a 40 μm thick photoresist (AZ 40 XT 11D) mask with 100 μm wide trenches [Figs. 2(d) and 2(e)]. Specifically, we performed an anisotropic etching for the SiO_2-Si_3N_4-SiO_2 stack—which is the material of our tip—using a $CF_4/Ar/O_2$ gas chemistry with 35/15/10 SCCM ratio, 20 mTorr of pressure, 20 °C of table temperature, 400 W of very high frequency (VHF) power, and 150 W of RF power in an Oxford Plasma Lab 100 Viper tool.

Then, when we reached the silicon layer, we changed to an isotropic silicon etch to remove, in a controlled way, the silicon underneath the tip and, at the same time, to release the final device. We used SF_6 and O_2 (24 and 26 SCCM, respectively), 20 °C, 6 mTorr, and 700 W of an inductively coupled plasma (ICP), and 20 W of RF power in an ICP RIE (Oxford PlasmaLab 150 ICP). More details on this last fabrication step are given in Appendix C. The sidewall profile control is critical during the silicon etch to ensure its complete removal underneath the probe's tip. For example, Figs. 2(f) and 2(g) show a scanning electron microscope (SEM) cross section image of the probe's tip after anisotropic silicon etching [Fig. 2(f)]—resulting in a vertical sidewall profile compared to an isotropic etching [Fig. 2(g)], resulting in the continuous removal of silicon from the probe's sidewalls. Thus, the silicon is gradually consumed underneath the probe's tip but is left unaffected underneath larger probe areas, as shown in Figs. 2(h) and 2(i).

III. RESULTS

A. Mechanical characterization in air

Invasive probes generate acute tissue damage during device insertion—damage correlated with the tip's cross-sectional dimension[37]—and after device insertion due to brain micromotions around stiff devices.[26] Here, we reduced both (1) the tip's cross

Published under an exclusive license by the AVS

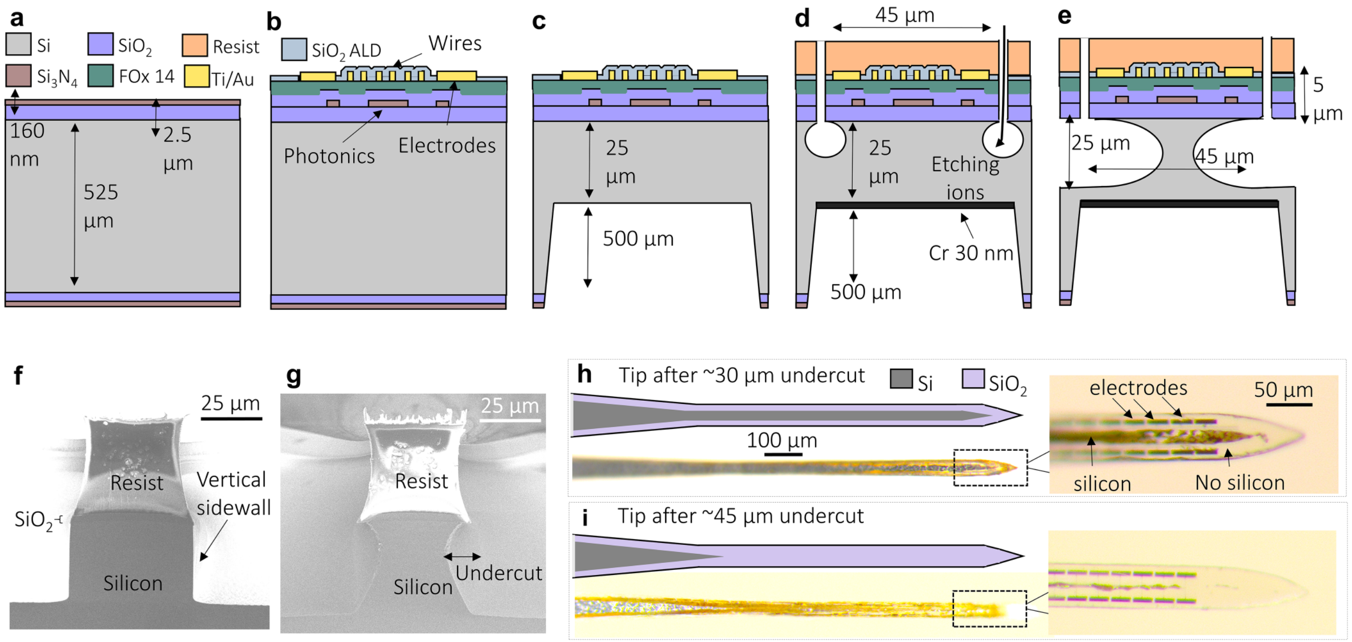

FIG. 2. Probe nanofabrication. (a)–(e) Schematic of the nanofabrication process, showing (a) the starting wafer, (b) the photonic patterning and planarization, (c) electrode and interconnection patterning, (d) thinning of the interconnecting and tip areas, and (e) etching of the probe's shape and simultaneous removal of the silicon underneath the probe's tip. (f)–(g) Comparison of (f) dry anisotropic etching that yields vertical sidewalls and (g) comparison with isotropic silicon etching to remove the silicon underneath the oxide. (h)–(i) Schematic and top-view optical microscope images of the probe's tip during silicon removal, after (h) ~30 μm and (i) 40 μm of total undercut in the silicon.

section and (2) its bending stiffness along the thickness axis by removing the silicon layer underneath the probe's tip.

(1) Our resulting tip's cross section is only 225 μm^2 (45 μm width × 5 μm thickness), which is smaller than several other state-of-the-art optoelectrodes.[15,18,19] Additionally, the tip's lateral dimension (45 μm width) can be further decreased: photonics occupy a lateral footprint as low as 15 μm (Ref. 15), while interconnections and electrodes occupy 40 μm, with the possibility of reducing the latter's footprint by either decreasing the interconnection pitch (currently 450 nm) or by integrating interconnections onto multiple layers.
(2) The probe's bending stiffness along the thickness direction ($J = 4.4 \times 10^{-11}$ N m^2)[38,39] of our silicon oxide-nitride-oxide tip can be calculated with the following formula:

$$J = \frac{h^3 \times E \times w}{12 \times (1 - \sigma)},$$

where h is the probe's thickness, w is the lateral width, E is Young's modulus, and σ is Poisson's ratio ($0 < \sigma < 1$).

Polymeric probes consist of low Young modulus materials (E ~ 1–20 GPa[26]) but have typically bulky and nonscalable dimensions (~tens of μm), especially in the presence of polymeric waveguides, which have large cross-sectional dimensions (~tens of μm × tens of μm).[27,28] As a result, our 1 mm long, 45 μm wide, and 5 μm thick tip has a bending stiffness of $J = 4.4 \times 10^{-11}$ N m^2, which is lower than state-of-the-art silicon and nitride optoelectrodes [$J = 4.3 \times 10^{-8}$ N*m^2 (Ref. 18) and $J = 4.9 \times 10^{-9}$ N m^2 (Ref. 15)] and approaching state-of-the-art polymeric optoelectrodes [i.e., J~1.7×10^{-12} N m^2 (Ref. 27), as described in Appendix A]. At the same time, we retained the capabilities of silicon-based devices to integrate a high number of electrodes (64 in our current design) and high-density and scalable silicon nitride photonics.

After microfabricating the probes, we noticed that the tip is bent, probably due to residual stress in various layers (SiO_2, Si_3N_4, SiO_2, FOx planarization, and SiO_2 passivation). However, we did not notice a significant stress tip deflection difference between the presence or the absence of metal lines. To insert the device's tip in brain tissue, we needed a straight tip. An initial way to achieve this is by careful layer stress calibration; however, high-quality optical layers often have high intrinsic stress, whose fine-tuning by process recipe change may degrade the layer's optical quality and increase optical absorption. A secondary way to modify the probe's tip stress is by using a heat treatment, which, for microcantilevers made of stacks of different materials, results in beam deflection due to a differential change of the materials' expansion or compression.[40,41] Our probe's tip integrates different materials (LPCVD SiO_2 and Si_3N_4, PECVD and ALD SiO_2); after a 20 min heat treatment in an oven, we change the tip bending, as shown in Figs. 3(a)–3(f). Thus, for a fixed time (20 min) and low temperatures (<150 °C), we can compensate for the tip's initial

Published under an exclusive license by the AVS

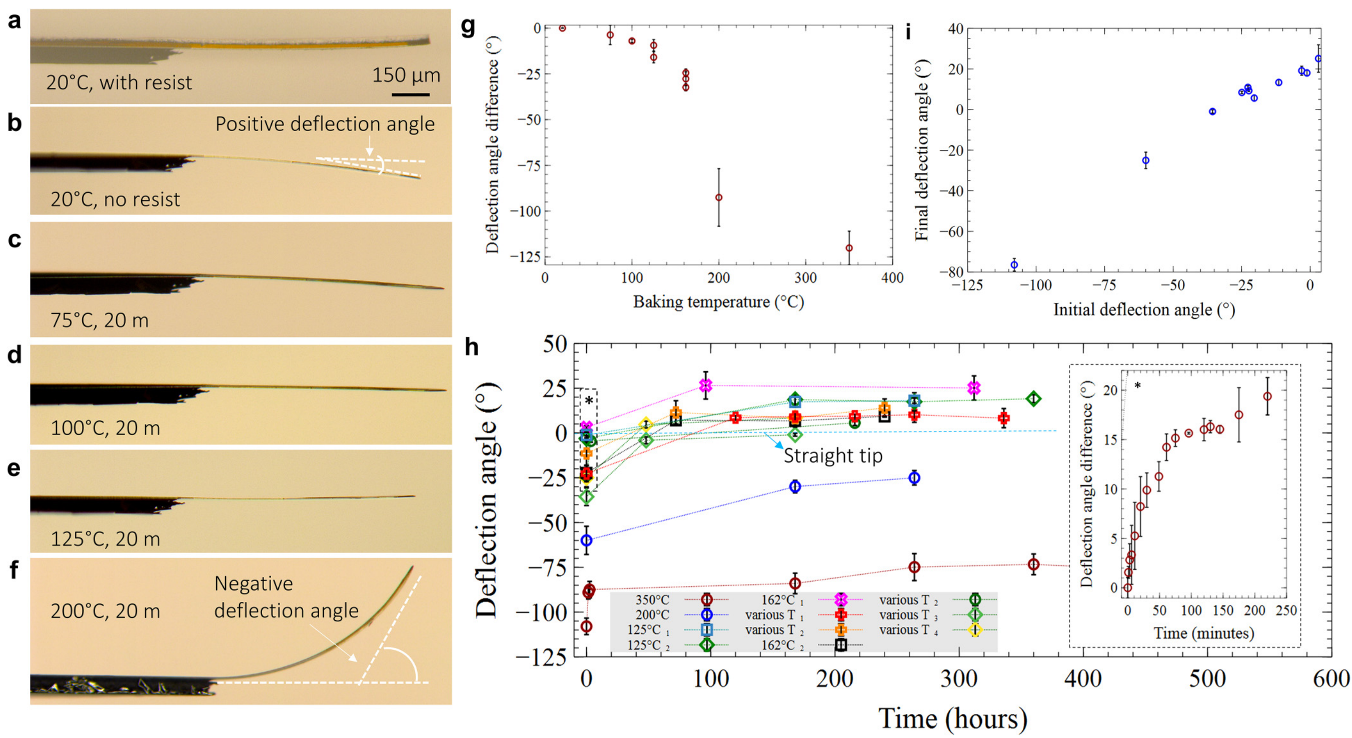

FIG. 3. Probe mechanical characterization. (a)–(f) The probe deflection angle, which stems from nonbalanced stresses between the layers, can be compensated by heating the probe. (g) Plot showing the experimental tip deflection angle change (the tangential angle difference with respect to the angle before baking) in degrees (°) as a function of baking temperature in degree Centigrade (°C) at a fixed time (20 min). (h) The tip deflection—in degrees, (°)—changes over time until it reaches a steady-state angle, with a quick angle change over the first few hours (inset); this steady-state angle depends on (i) the initial beam deflection [also in degrees, (°)]. Thus, it is possible to choose the initial angle to achieve a steady-state angle of 0° (straight tip).

deflection angle [Fig. 3(g)]. After heating the probes, we removed them from the oven and let them cool down at room temperature (20 °C) for 3 min. Then we measured the tip's deflection over time (always at 20 °C), and we noticed that after an initial change over the first few hours [Fig. 3(h), inset], the induced deflection does not change significantly over time [Fig. 3(h)] and is correlated to the initial angle after heating [Fig. 3(i)]. These results point to the capability of performing an annealing step to impart plasticity and obtain a straight tip. Future work will assess the exact reason for tip bending by measuring the layers' stresses and how they change with temperature variations during the device fabrication process and after the final annealing process.

B. Optical and *in vitro* mechanical characterization

After obtaining straight probe tips, we characterized their angle change after soaking them in saline solution at 37 °C to mimic the brain's ionic environment, and we tested the photonics' performance and compare it to our previous results.[15,16]

First, we measured changes in the deflection of several tips before, during, and after soaking them in saline solution heated at 37 °C [Figs. 4(a)–4(d)]. We calculated the tip's deflection angle in saline at different times and compare it to the tip's deflection before saline soak [Fig. 4(e)], showing an angle change of a few degrees shortly after (<5 min) soaking the probes in saline ($3.42 \pm 1.88°$) and a slow increase over 2 h for probe 2 and 3 or a constant angle for probes 1, 4, and 5. After soaking a probe for 240 min in a saline solution, we lifted it in the air [Fig. 4(d)], measured the tip's deflection angle, and compared it to both probes: the probe in the air before saline soak from Fig. 4(a) (angle change: $2.71 \pm 0.39°$) and the one in saline at 240 min (angle change: $-3.06 \pm 1.26°$).

Overall, these measurements show that tips bend by just a few degrees in saline throughout short-term experiments (few hours). However, the tip deflection could pose challenges for long-term chronic animal experiments as it could cause stress to brain tissue and difficulty in tracking the same neurons over time.

Then, we characterized the probe's photonics' performance by aligning the external laser's optical fiber to the waveguide input in the probe interface area while monitoring the grating outputs in the tip with a microscope [Figs. 4(f)–4(h)].

We fabricated rings as an example of photonics to deliver light in desired areas[15,16]; however, our device can integrate other photonic circuits—such as arrayed waveguide gratings,[24] multimode interference splitters,[42] or thermally tuned Mach–Zehnder interference switches.[19]

Published under an exclusive license by the AVS

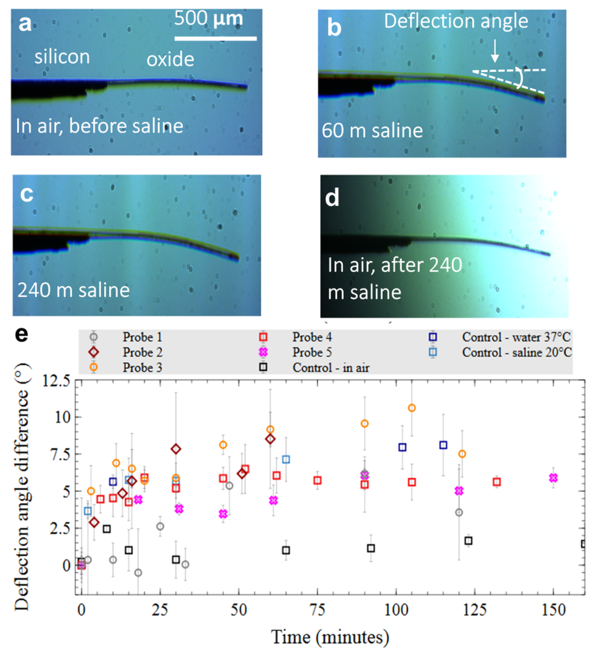

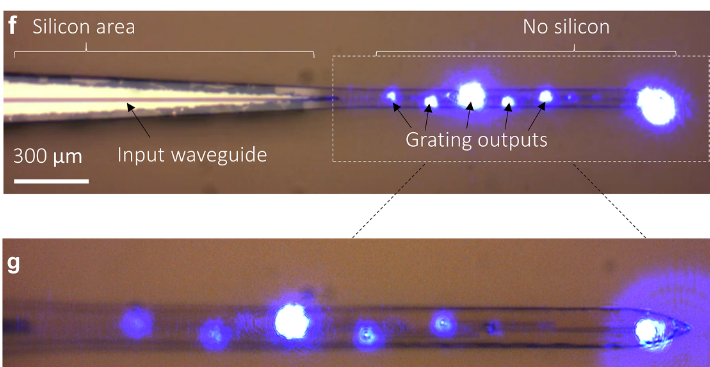

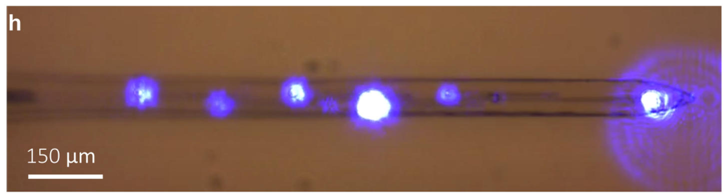

FIG. 4. Probe *in vitro* mechanical and optical test. (a)–(d) Optical microscope images of the probe's tip (a) before, (b) and (c) during, and (d) after saline soaking at different times. The (e) angle change—in degrees (°)—with respect to the tip angle in the air is plotted as a function of time and shows a slight angle deflection with little change over times longer than 2 h, comparable with an *in vivo* acute experiment time. (f)–(h) Optical characterization: we aligned an optical fiber to the waveguide's input and tune the external laser's wavelength to select different resonators, similarly to what we showed in (Refs. 14 and 20). Images are oversatured for graphical purposes.

We validated the ring resonators in our previous works[15,16]; here, we measured ring coupling efficiencies between 62% and 77% and cross-talk values (the percentage of light going to nonselected sites) of $6.3 \pm 2\%$. This cross-talk value may prevent the activation of opsins near nonselected sites by fine-tuning the grating output power.[15,16] These optical measurements are slightly different from our previously published results (coupling between 45% and 60% and cross talk $5.2 \pm 2.6\%$[15]), which we hypothesize arising due to stoichiometry variations when depositing the PECVD top cladding rather than from the absence of silicon (since the bottom and top cladding are $2.5\,\mu$m thick).

Besides, we previously showed that our system was performant enough to activate brain opsins, which have a typical activation threshold of around $1\,\mathrm{mW/mm^2}$ (Ref. 43), while here we measured an output power density around $1500\,\mathrm{mW/mm^2}$ (using a 10 mW laser input power).

C. *In vivo* probe insertion

Finally, we performed some proof of concept *in vivo* insertion experiments to demonstrate that our device can penetrate rat pia without using additional rigid supports[38,44–46] that can have large cross sections that result in additional insertion damage and the dissolution of biodissolvable glue in brain tissue.

Even though our probes have ultralow bending stiffness ($4.4 \times 10^{-11}\ \mathrm{N\,m^2}$), they can penetrate rat pia without coupling to external rigid supports. We perform seven insertions in two different rats. In brief, we performed craniotomy in rats to remove part of the skull and dura and expose the pia. We then lowered the probe vertically with either a manual micrometer or a piezo-actuator (PZA-12, by Newport) while monitoring the tip-brain interface with a microscope and a CCD camera, as shown in Fig. 5. More details on the rat preparation and setup are given in Appendix F.

The first two insertions where we lowered probes with bent tips using the manual translation stage failed, leading to the oxide part of the probe breaking at the interface with the silicon. However, the insertions in the rats where the piezo-actuator lowered the probes were successful. In particular, we noticed probe buckling before piercing the pia for probes with initially bent tips but negligible buckling for probes with the initial straight tip. The last four insertions were performed using the same probe, demonstrating that our probes can be used multiple times before breaking.

Thus, we demonstrated that our probes with an unbending angle could successfully penetrate rat pia multiple times before breaking and without external rigid supports, which would increase the damage to brain tissue.

IV. DISCUSSION

We have described the design, nanofabrication, some *in vitro* mechanical and optical characterizations, and preliminary *in vivo* insertions of a device merging the scalability of silicon nitride optoelectrodes with the low bending stiffness typical of polymers for

Published under an exclusive license by the AVS

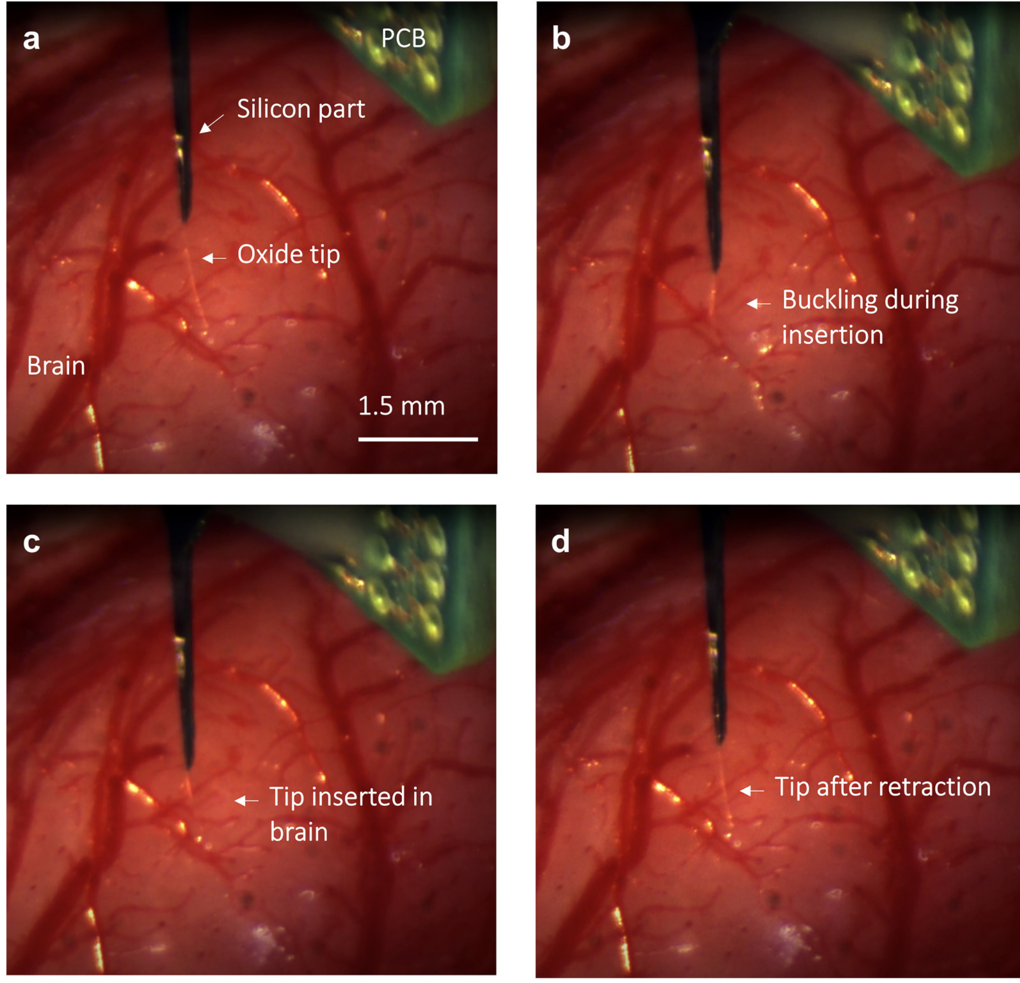

FIG. 5. Proof of concept *in vivo* insertion experiment. We show the insertion of the probe's tip in the brain without the use of rigid supports or biodissolvable glue. (a) Probe tip before, (b) during—showing buckling—and (c) after insertion and (d) retraction.

acute and high-resolution *in vivo* studies. Starting from a high-density silicon optoelectrode[15,16] and by exploiting a single isotropic silicon etch step, we remove all of the silicon underneath the probe's tip area, thus yielding tip with 45 μm lateral width and only 5 μm thickness—while leaving the rest of the device unaffected for ease of handling and packaging. Based on our initial objective of studying the mouse cortex, we chose the tip's length to be 1 mm. Longer tips (i.e., 5 mm) can be fabricated with the same processes described in Secs. I–III and more careful material stress compensation and implantation strategies.

Since our nanofabrication approach relies on standard semiconductor micro- and nanofabrication techniques, it allows for fabricating probes with high throughput, scalability, high material thickness precision, and integrating multiple layers with different functions, i.e., photonic and electrical. Our probe integrates the same high-density electrodes and passive silicon nitride photonics of our previously published devices[15,16] while reducing the cross section significantly (from 900 to 225 μm^2) and the bending stiffness along the probe's thickness direction (from 4.9×10^{-9} to 4.4×10^{-11} N m^2), approaching the one of state-of-the-art polymeric optoelectrodes. In addition to low bend stiffness, we demonstrated that we could insert our device without coupling it to temporary rigid supports, resulting in a device cross section as small as 225 μm^2 during insertion.

While the probe could lead to a high spatial and temporal resolution readout and manipulation of neural activity with minimal tissue damage thanks to the combination of a high number of electrodes, passive and addressable photonics, and superthin cross section dimensions and flexibility, we envision its use for short-term (< hours to days) interrogations of neural networks.

Further work is needed to evaluate whether longer durations in brain tissue could lead to an increased probe deflection and could

Published under an exclusive license by the AVS

limit the capability of tracking neurons or induce additional brain damage. Furthermore, while silicon dioxide was shown to be a biocompatible material with excellent properties as a biofluid barrier, it is expected to slowly dissolve with a rate of 0.08–8 nm/day,[47–49] which could further affect the probe's stress and bending.

Future work will aim to scale the tip's lateral dimension, which is mainly limited by the interconnections' and electrodes' lateral footprint (40 μm in total) and reduce the wire pitch (while photonics occupy a lateral footprint as low as 15 μm). We will also measure the tip's buckling force during insertion and perform additional *in vivo* insertions to provide statistical results concerning the insertion reliability of a single tip for multiple insertions in a target brain region. We would like to integrate additional layers above (or below) the electrodes to add new functions (i.e., microfluidics) and test *in vivo* the electrodes (which, in our current configuration, need for packaging optimization, as we describe in the Appendix G). Finally, we will validate the probe's viability for chronic studies.

In conclusion, this work demonstrated the capabilities of embedding the high sensor and light emitter density of silicon probes, scalability, and throughput with the flexibility typical of polymeric optoelectrodes using a single isotropic silicon etch step. We thus show substantial advancement in the technological field of neural optoelectrodes in terms of the combination of scalability, sensor and passive light emitter density, and acute damage reduction.

AUTHORS' CONTRIBUTIONS

V.L. was the leading researcher managing and working on the entire project. He conceived the project idea and designed, simulated, fabricated, optimized, assembled, and experimentally *in vitro* characterized the neural probes. V.G. and J.H. performed the *in vivo* experiment, supervised by K. Bouchard. The manuscript writing, data interpretation, and discussion were done by V.L. S.C. supervised V.L.'s work.

ACKNOWLEDGMENTS

The authors would like to thank Andrea Lamberti and Fabrizio Pirri for their technical advice, Gregory Telian and Hillel Adesnik for preliminary probe insertion in mouse, Scott Dhuey for electron beam lithography exposures, and Komal Kampasi and Peter Denes for technical advice. Work at the Molecular Foundry was supported by the Office of Science, Office of Basic Energy Sciences, of the U.S. Department of Energy under Contract No. DE-AC02-05CH11231. The authors declare no conflict of interest. The work has not been published or submitted for publication elsewhere, and no materials are reproduced from another source.

APPENDIX A: COMPARISON WITH STATE-OF-THE-ART OPTOELECTRONIC DEVICES

We compare our probe with several state-of-the-art brain implantable optoelectrical devices (Table I and Fig. 6) that combine low bend stiffness and cross-sectional area coefficient (CSAC). These devices, which interface with large numbers of neurons with minimal brain implantation damage, encompass silicon-based and polymeric Michigan probes integrating waveguiding structures or micro-light-emitting diodes, tapered and multifunctional fibers, and mesh probes. For each work, we estimated the bending stiffness and CSAC, showing that the thin glass-nitride probe combines low bending stiffness and CSAC.

TABLE I. Examples of state-of-the-art optoelectric brain invasive devices combining low bending stiffness and low cross-sectional area coefficient (CSAC). For different works, we report the substrate, waveguide cladding, and waveguide core materials (S, Cl, and Co); the tip width (W, in μm) times height (H, in μm); the number of electrodes (E) and optical sites (O); the bending stiffness along the thickness direction (B, in N m^2); the CSAC (in μm^2); the illumination type (I).

Work	S, Cl, and Co	W × H	E,O	B	CSAC	I
Probe with rings[15,16]	Si, SiO_2, and Si_3N_4	45 × 20	64, 6	4.9×10^{-9}	12.8	Passive, addressable
This work	No substrate, SiO_2, and Si_3N_4	45 × 5.2	64, 6	4.4×10^{-11}	3.1	Passive, addressable
High-density optoelectrode[18]	Si, SiO_2, and Si_3N_4	100 × 30	24, 12	4.3×10^{-8}	83.3	Passive, addressable
Polymeric opto-electro mechanical systems[27]	No substrate, Cytop, and OrmoClearFX/EpoCore	80 × 5 (Cl); 10 × 10 (Co)	8, 1	1.7×10^{-12}	61.1	Single point
Tapered fibers[31,32]	SiO_2 and SiO_2	Diameter: ∼60 μm[a]	0, 7	1×10^{-7}	1742.3	Passive, addressable
Probe with micro-LEDs[12,13,50,51]	Si (doped), MicroLED: GaN, GaN/In, and GaN multiquantum well	70 × 30	64, 32	3×10^{-8}	21.8	Addressable, nonpassive
Multifunctional fibers[52]	Cyclic olefin copolymer, and polycarbonate	Diameter: 70 μm	7, 1	2×10^{-9}	1932.2	Single point
Multifunctional optoelectronic mesh[29]	SU-8, no clad, and SU-8	20 × 1[b]	16, 1	$<10^{-14}$	27.05	Single point

[a]The bending stiffness of Refs. 31 and 32 was roughly estimated by considering the diameter at the taper's midpoint (∼60 μm).
[b]The bending stiffness of Ref. 29 was roughly estimated (but may be much lower) by considering the sum of 16 vertical beams (one per electrode) and 9 horizontal beams in between with 20/10 μm width and 1 μm thickness.

Published under an exclusive license by the AVS

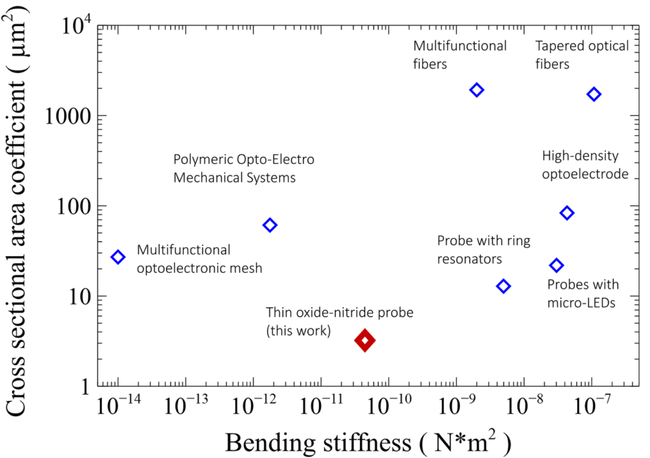

FIG. 6. Plot comparison of examples of state-of-the-art electro-optic brain invasive devices combining low bending stiffness and low cross-sectional area coefficient.

APPENDIX B: DOUBLE SIDE EMISSION DUE TO THE TIP'S TRANSPARENCY

While regular silicon optoelectrodes allow for illuminating only above the grating (due to the reflective silicon layer underneath), our gratings emit on both sides (upward and downward) and thus provide illumination on a broader tissue volume, which could be useful when illuminating 360° symmetric structures such as cortical columns.[53]

As for our other works (Refs. 13, 14, and 20), we design gratings with 4 μm width, 15 μm length, 315 nm pitch, and 50% duty cycle [Fig. 7(a)]. Figure 7(c) is a finite time difference domain (FDTD, Lumerical) simulation comparing the grating's up and down transmission, which shows similar efficiency. Figures 7(d) and 7(e) show the grating's far-field emission, demonstrating that the up and down beams are collimated. Other types of beam shape can be achieved depending on the emission of interest (i.e., beam focusing,[17] long-distance collimation,[24,54] etc.).

APPENDIX C: SILICON ANISOTROPIC AND ISOTROPIC ETCH

We defined the undercut ratio as the amount of material removed from the sidewall divided by the material removed at the bottom of the trench during the silicon etch. Thus, an undercut ratio of 0 represents an anisotropic/vertical etch, while a value of 1 an isotropic/chemical etch. In Fig. 8, we show some examples of undercut ratios for SF_6/O_2 and SF_6/C_4F_8 gas chemistries and with different substrates (1-in. wafer pieces, entire wafer, entire wafer with 20 μm thick and 1 cm^2 area membranes) and resists (1.5 μm thick MAP1215 and 40 μm thick AZ40XT-11D). Silicon etch rates and undercut were measured by cleaving the samples after etching and imaging their cross section in a scanning electron microscope.

Samples with Sf_6/O_2 were etched in an Oxford PlasmaLab 150 ICP tool with 35 W of RF, 300 W of ICP, and 20 mTorr pressure. 1-in. side pieces were mounted with Fomblin oil on a 4-in. silicon wafer with a chromium mask to avoid microloading effects, resulting in straight sidewalls at high SF_6 gas ratios (black circles in Fig. 8).

Samples etched with SF_6/C_4F_8 gas were processed in an Oxford Plasma Lab 100 Viper tool with 35 W RF, 300 W VHF, and 20 mTorr of pressure; 1-in. pieces and wafers were mounted with Fomblin oil on top of an 8-in. silicon wafer.

Low SF_6 concentrations give lower undercut, especially for SF_6 mixed with C_4F_8 (although there may be some loading effects for the latter due to using a silicon carrier). On the other end, a high undercut ratio can be achieved by using SF_6/O_2 gases and etching

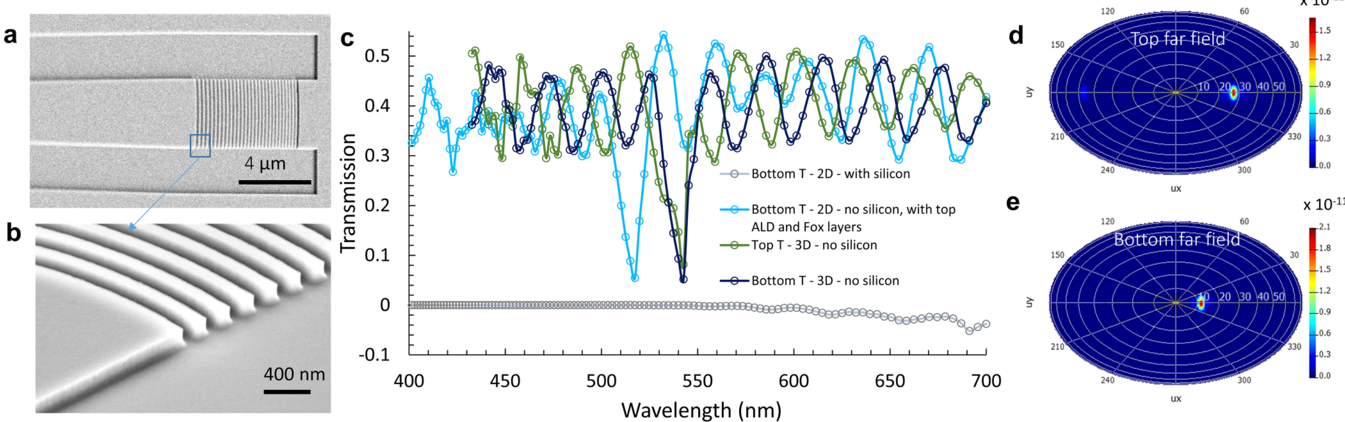

FIG. 7. Grating for double side emission. (a) and (b) Scanning electron microscope image of the grating [(a) top view; (b) magnified tilted view] before SiO_2 cladding. (c) Grating normalized emission both up and down and with/without silicon. (d) and (e) Grating far-field emission (450 nm wavelength) above and below the grating for probes without silicon. Units are calculated by integration over the whole emission sphere. The corresponding efficiency is shown in (c); the calculated output power is around 1.5 W/mm^2.

Published under an exclusive license by the AVS

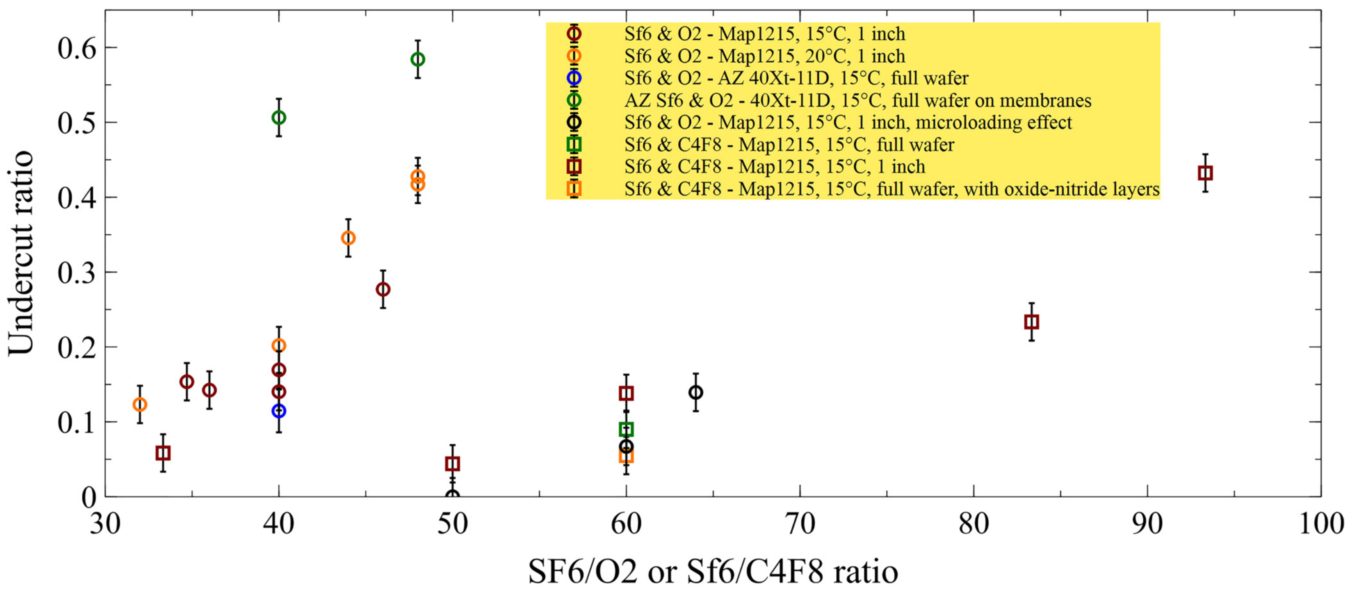

FIG. 8. Undercut ratio during silicon etch for different gas chemistries, substrates, and resists. Changing the recipe parameters makes it possible to achieve either low or high undercut ratios (vertical sidewall or isotropic etching, respectively).

the wafer where probes were patterned on top of 20 μm thick membranes (green circles).

Other gases, pressures, RF and ICP powers, and temperatures can be used to fine-tune the etching process further.

APPENDIX D: OPTICAL SETUP

Measurements from Figs. 3(a)–3(h) were performed by imaging the probe in a lateral view with a microscope and CCD. Angle deflection measurements are taken with ImageJ software, with multiple measurements for each image to average out errors. Similarly, *in vitro* measurements from Figs. 4(a)–4(g) were performed by imaging the probe with a microscope and a CCD camera before and after immersion in a beaker of saline heated at 37 °C and at different times. The temperature was kept constant using a thermocouple.

Optical measurements from Figs. 4(h)–4(j) were taken with a microscope and a CCD camera after edge coupling a single-mode fiber (SM 400, from Thorlabs) to the probes' waveguide inputs. As an input light source, we use a 450 nm laser (QFLD-450-10S, from QPhotonics). More details were given in our previous works.[15,16] All the probes used for these measurements did not have the planarization FOx layer.

APPENDIX E: BUBBLES ON SILICON

Bubbles were noticed on all probes soaked in saline solution at 37 °C only in areas of the probe with silicon. Interestingly, we noticed no bubbles on oxide areas (Fig. 9). Further studies will be performed to assess whether the bubble formation happens inside living brains and whether it impacts neural recordings.

APPENDIX F: RAT PREPARATION

All rat procedures were performed in accordance with established animal care protocols approved by the Lawrence Berkeley National Laboratory, Institutional Animal Care and Use Committees (IACUC). We performed acute craniotomy experiments in both female and male Sprague Dawley rats (CD-1, Charles River Laboratories). The animals were under a brief flow of 2% isoflurane before being given an inductive dose of ketamine (90 mg/kg i.p.) and xylazine (10 mg/kg i.p.) to induce an anesthetic state. A toe pinch reflex method and periodic monitoring of the respiration rate were assessed to maintain the anesthetic state. Additional doses of ketamine (55 mg/kg i.p) and xylazine (5 mg/kg i.p.) were conducted as needed to conserve a negative reflex and a consistent reduced respiration rate. Respiration was supported with a perioperative nose cone supplying 1.0 l/min of O_2. A water heating pad of 37 °C provided thermoregulation. To prevent dehydration, subcutaneous saline injections (1 ml/kg) were provided every 2 h.

Once anesthetized and stable, the animals were affixed to a snout stereotaxic frame without ear bars. An incision was made along the sagittal midline. All the soft tissues on top of the skull were removed to reveal the lambda and bregma fissures. Two 1 mm burr holes were drilled using a 1 mm round dental drill—one above bregma on the left hemisphere and another above bregma on the right hemisphere. These assist in reducing intracranial pressure. The

Published under an exclusive license by the AVS

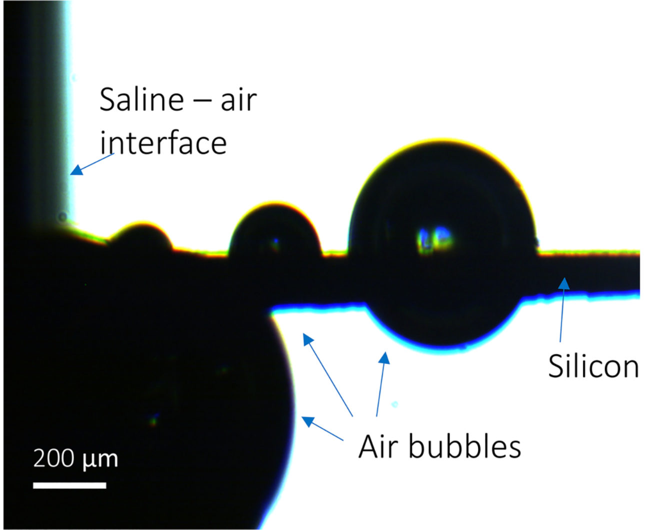

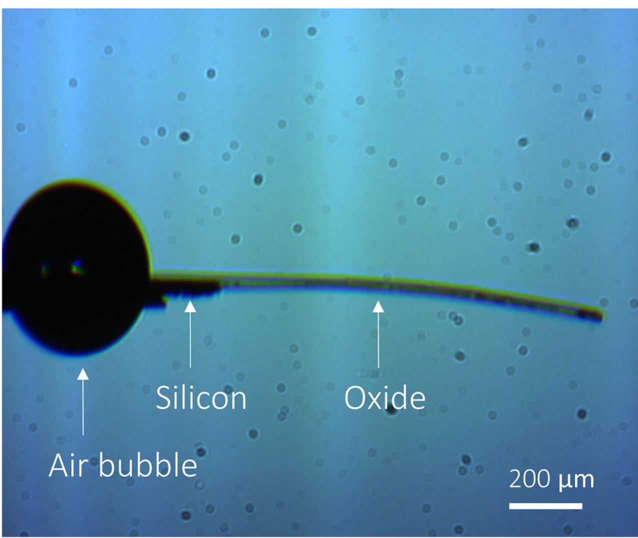

FIG. 9. Lateral view of the probe interconnecting and tip areas immersed in saline solution at 37 °C, showing bubble formation on silicon but not on oxide.

right masseter muscle was then transected to reveal a segment of cranium over the right auditory cortex. A craniotomy window was drilled to uncover the cortex. Finally, the dura mater was removed.

APPENDIX G: ELECTRICAL ASSEMBLY

An electrical connection between the optoelectrode and the PCB was performed by automatic wire bonding assisted by ultrasound in our previous works.[15,17] Here, we noticed that the oxide tip breaks off when we bond the internal electrodes but not the external ones [as indicated in Figs. 10(a) and 10(b)]. We think this may be due to vibration propagation from the probe interface area to the oxide-silicon interface areas [Fig. 10(c)]. Therefore, future work will

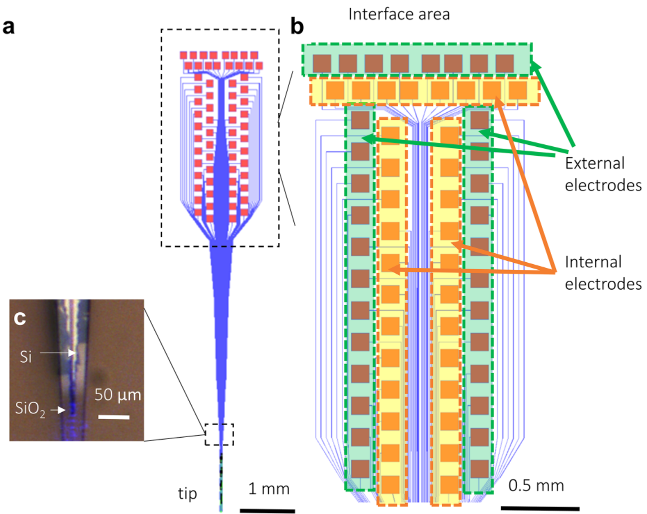

FIG. 10. Probe design, showing (a) and (b) the probe and electrodes for PCB electrical connection and (c) the silicon-oxide interface area, where silicon terminates with a sharp geometry.

either use wire bonding without ultrasound or other techniques (i.e., flip-chip bonding or techniques like those shown in[27]) or redesign the silicon-oxide interface areas to avoid terminating the silicon part with a sharp tip.

DATA AVAILABILITY

The data that support the findings of this study are included within the article.

REFERENCES

[1]E. Musk, J. Med. Internet Res. **21**, e16194 (2019).
[2]E. Krook-Magnuson, G. G. Szabo, C. Armstrong, M. Oijala, and I. Soltesz, eNeuro **1**, ENEURO.0005-14.2014 (2014).
[3]U. Chaudhary, N. Birbaumer, and A. Ramos-Murguialday, Nat. Rev. Neurol. **12**, 513 (2016).
[4]Z. J. Huang and L. Luo, Science **350**, 42 (2015).
[5]G. Hong and C. M. Lieber, Nat. Rev. Neurosci. **20**, 330 (2019).
[6]X. Liu, S. Ramirez, and S. Tonegawa, Philos. Trans. R. Soc. B Biol. Sci. **369**, 20130142 (2013).
[7]Z. Fekete, Sensors Actuators B Chem. **215**, 300 (2015).
[8]G. Buzsáki, E. Stark, A. Berényi, D. Khodagholy, D. R. Kipke, E. Yoon, and K.D. Wise, Neuron **86**, 92 (2015).
[9]C. K. Kim, A. Adhikari, and K. Deisseroth, Nat. Rev. Neurosci. **18**, 222 (2017).
[10]N. McAlinden, D. Massoubre, E. Richardson, E. Gu, S. Sakata, M. D. Dawson, and K. Mathieson, Opt. Lett. **38**, 992 (2013).
[11]N. Dong, R. Berlinguer-Palmini, A. Soltan, N. Ponon, A. O'Neil, A. Travelyan, P. Maaskant, P. Degenaar, and X. Sun, J. Biophotonics **11**, e201700358 (2018).
[12]F. Wu, E. Stark, Pei-Cheng Ku, K. D. Wise, György Buzsáki, and Euisik Yoon, Neuron **88**, 1136 (2015).
[13]K. Kim *et al.*, bioRxiv (2020).
[14]F. Pisanello, L. Sileo, and M. De Vittorio, Front. Neurosci. **10**, 1 (2016).
[15]V. Lanzio *et al.*, Microsyst. Nanoeng. **7**, 40 (2021).

Published under an exclusive license by the AVS

[16]V. Lanzio, M. Lorenzon, S. Dhuey, C. F. Pirri, A. Lamberti, and S. Cabrini, Nanotechnology **32**, 265201 (2021).
[17]V. Lanzio, Melanie West, Alexander Koshelev, Gregory Telian, Paolo Micheletti, Raquel Lambert, Scott Dhuey, Hillel Adesnik, and Simone Sassolini, J. Micro/Nanolithogr. MEMS MOEMS **17**, 1 (2018).
[18]S. Libbrecht, Luis Hoffman, Marleen Welkenhuysen, Chris Van den Haute, Veerle Baekelandt, Dries Braeken, and Sebastian Haesler, J. Neurophysiol. **120**, 149 (2018).
[19]A. Mohanty *et al.*, Nat. Biomed. Eng. **4**, 223 (2020).
[20]E. Shim, Y. Chen, S. Masmanidis, and M. Li, Sci. Rep. **6**, 6 (2016).
[21]N. C. Klapoetke *et al.*, Nat. Methods **11**, 338 (2014).
[22]C. M. Lopez, Alexandru Andrei, Srinjoy Mitra, Marleen Welkenhuysen, Wolfgang Eberle, Carmen Bartic, Robert Puers, Refet Firat Yazicioglu, and Georges G. E. Gielen, IEEE J. Solid-State Circuits **49**, 248 (2014).
[23]C. Mora Lopez *et al.*, IEEE Trans. Biomed. Circuits Syst. **11**, 510 (2017).
[24]E. Segev *et al.*, Neurophotonics **4**, 011002 (2016).
[25]M. A. Hopcroft, W. D. Nix, and T. W. Kenny, J. Microelectromech. Syst. **19**, 229 (2010).
[26]A. Lecomte, E. Descamps, and C. Bergaud, J. Neural Eng. **15**, 031001 (2018).
[27]K. Kampasi, I. Ladner, J. Zhou, A. C. Soto, J. Hernandez, S. Patra, and R. U. Haque, Mater. Lett. **285**, 129015 (2021).
[28]K. Kampasi, Daniel F. English, John Seymour, Eran Stark, Sam McKenzie, Mihály Vöröslakos, György Buzsáki, Kensall D. Wise, and Euisik Yoon, Microsyst. Nanoeng. **4**, 1 (2018).
[29]J. M. Lee, Dingchang Lin, Ha-Reem Kim, Young-Woo Pyo, Guosong Hong, Charles M. Lieber, and Hong-Gyu Park, Nano Lett. **21**, 3184 (2021).
[30]L. Sileo *et al.*, Front. Neurosci. **12**, 771 (2018).
[31]F. Pisanello, L. Sileo, I. A. Oldenburg, M. Pisanello, L. Martiradonna, J. A. Assad, B. L. Sabatini, and M. De Vittorio, Neuron **82**, 1245 (2014).
[32]F. Pisanello *et al.*, Nat. Neurosci. **20**, 1180 (2017).
[33]F. Deku *et al.*, Micromachines **9**, 480 (2018).
[34]F. Deku, Y. Cohen, A. Joshi-Imre, A. Kanneganti, T. J. Gardner, and S. F. Cogan, J. Neural Eng. **15**, 016007 (2018).
[35]R. G. Heideman, A. Leinse, M. Hoekman, F. Schreuder, and F. H. Falke, "TriPleX™: The low loss passive photonics platform: Industrial applications through Multi Project Wafer runs," *2014 IEEE Photonics Conference*, San Diego, CA, 12–16 October 2014 (IEEE, 2014), pp. 224–225.
[36]R. A. Rahim, B. Bais, B. Y. Majlis, and G. Sugandi, Microsyst. Technol. **19**, 905 (2013).
[37]D. H. Szarowski, M. D. Andersen, S. Retterer, A. J. Spence, M. Isaacson, H. G. Craighead, J. N. Turner, and W. Shain, Brain Res. **983**, 23 (2003).
[38]X. Yang, Tao Zhou, Theodore J. Zwang, Guosong Hong, Yunlong Zhao, Robert D. Viveros, Tian-Ming Fu, Teng Gao, and Charles M. Lieber, Nat. Mater. **18**, 510 (2019).
[39]K. Najafi, J. Ji, and K. D. Wise, IEEE Trans. Biomed. Eng. **37**, 1 (1990).
[40]W. Fang, H. C. Tsai, and C. Y. Lo, Sens. Actuators A Phys. **77**, 21 (1999).
[41]C.-Y. Lee, C.-H. Tsai, L.-W. Chen, L.-M. Fu, and Y.-C. Chen, Microsyst. Technol. **12**, 979 (2006).
[42]F.-D. Chen *et al.*, Neurophotonics **8**, 025003 (2021).
[43]X. Han, ACS Chem. Neurosci. **3**, 577 (2012).
[44]S. H. Felix, K. G. Shah, V. M. Tolosa, H. J. Sheth, A. C. Tooker, T. L. Delima, S. P. Jadhav, L. M. Frank, and S. S. Pannu, JoVE J. e50609 (2013).
[45]S. Zhang, C. Wang, C. Linghu, S. Wang, and J. Song, J. Appl. Mech. Trans. ASME **88**, 010801 (2021).
[46]F. Ceyssens *et al.*, Sens. Actuators B Chem. **284**, 369 (2019).
[47]S. K. Kang *et al.*, Nature **530**, 71 (2016).
[48]Y. K. Lee *et al.*, ACS Appl. Mater. Interfaces **9**, 42633 (2017).
[49]S.-K. Kang, Suk-Won Hwang, Huanyu Cheng, Sooyoun Yu, Bong Hoon Kim, Jae-Hwan Kim, Yonggang Huang, and John A. Rogers, Adv. Funct. Mater. **24**, 4427 (2014).
[50]F. Wu, E. Stark, M. Im, I. J. Cho, E. S. Yoon, G. Buzsáki, K. D. Wise, and E. Yoon, J. Neural Eng. **10**, 056012 (2013).
[51]K. Kim, M. Vöröslakos, J. P. Seymour, K. D. Wise, G. Buzsáki, and E. Yoon, Nat. Commun. **11**, 1 (2020).
[52]S. Park *et al.*, Nat. Neurosci. **20**, 612 (2017).
[53]F. Pisano, Marco Pisanello, Leonardo Sileo, Antonio Qualtieri, Bernardo L. Sabatini, Massimo De Vittorio, and Ferruccio Pisanello, Microelectron. Eng. **195**, 41 (2018).
[54]W. D. Sacher *et al.*, "Beam-steering nanophotonic phased-array neural probes," in *Conference on Lasers and Electro-Optics, OSA Technical Digest*, San Jose, California, 5–10 May 2019 (Optical Society of America, 2019), paper ATh4I.4.

Published under an exclusive license by the AVS